Received March 18, 2020, accepted March 31, 2020, date of publication April 9, 2020, date of current version April 30, 2020.

Digital Object Identifier 10.1109/ACCESS.2020.2986814

Research on Control Strategy for a Battery Thermal Management System for Electric Vehicles Based on Secondary Loop Cooling

XIJIN KUANG[1,2], KUINING LI[1,2], YI XIE[3], CUNXUE WU[3,4,5], PINGZHONG WANG[4,5], XIAOBO WANG[4,5], AND CHUNYUN FU[3]

[1]Key Laboratory of Low-grade Energy Utilization Technologies and Systems, Ministry of Education of China, Chongqing University, Chongqing 400044, China
[2]School of Energy and Power Engineering, Chongqing University, Chongqing 400044, China
[3]School of Automotive Engineering, Chongqing University, Chongqing 400044, China
[4]Chongqing Chang'an New Energy Automobile Technology Company Ltd., Chongqing 401120, China
[5]Chongqing Chang'an Automobile Company Ltd., Chongqing 401120, China

Corresponding author: Kuining Li (leekn@cqu.edu.cn)

This work was supported in part by the National Key Research and Development Program of China under Grant 2018YFB0106100, in part by NSF of China under Grant U1864212, and in part by the Major Program of Chongqing Municipality under Grant cstc2018jszx-cyztzxX0007.

ABSTRACT A secondary loop cooling battery thermal management system is designed, and then, a phased control strategy for adjusting the compressor speed according to the battery temperature interval is proposed. On this basis, the compressor speed as the decision variable, and the energy consumption of the compressor and the aging losses of the battery are as the optimization goals, which constitute a multi-objective optimization model, and a genetic algorithm is adopted to solve it. Under different weight coefficients, the Pareto Frontier of the energy consumption of the compressor and the aging losses of the battery are established. The simulation analysis is conducted on high speed dynamic conditions at an ambient temperature of 30 °C. The effects of coolant flow rate and compressor speed on battery pack temperature rise and temperature uniformity are analyzed. The simulation results show that the energy consumption of the phased control strategy is reduced by 10.7% compared with the traditional constant compressor speed control strategy under the same conditions. Under different weight coefficients, different simulation results and control strategies can be obtained, and results show that the maximum temperature and temperature uniformity can meet the requirements. There is a contradiction between the energy consumption of compressor and the aging losses of battery, but both them are highly sensitive. According to the Pareto Frontier curve, when the weight coefficient is 0.17, a balanced control strategy can be obtained, which can reduce the battery aging losses of 61.8% by only sacrificing 9.22% of the vehicle driving mileage.

INDEX TERMS Battery thermal management, control strategy, genetic algorithm, lithium-ion cell, multi-objective optimization, secondary loop cooling.

I. INTRODUCTION

In recent years, energy and environmental problems have become increasingly serious. Thus, electric vehicles have received increasing attention. The power battery is one of the core components of electric vehicles. Lithium-ion batteries are widely used as power batteries for electric vehicles because of their high energy and power densities, no memory effects, and long life [1]. However, lithium-ion batteries are susceptible to temperature. Studies have shown that [2] the suitable temperature range for lithium-ion batteries is 20–40 °C, and the maximum temperature difference in the battery pack should be less than 5 °C. Ramadass P *et al.* experimented with a cylindrical 18650 lithium-ion battery [3], and the results showed that the battery capacity decay was as high as 70% after 490 cycles at above 50 °C. Temperature not only affects the performance and life of lithium-ion batteries but also can cause safety problems. Therefore, it is very important to design a suitable battery thermal management system to control the temperature of the battery within a suitable range.

The methods of battery cooling mainly include air cooling [4], [5], liquid cooling [6], [7], phase change material cooling [8], [9] and heat pipe cooling [10], [11]. Zhao *et al.* [12]

The associate editor coordinating the review of this manuscript and approving it for publication was Zhiyi Li.

This work is licensed under a Creative Commons Attribution 4.0 License. For more information, see https://creativecommons.org/licenses/by/4.0/

studied the effects of the ventilation type, air flow rate, gap spacing, number of single-row cells, and ambient temperature on the heat dissipation performance of air-cooled systems. It was determined that when the wind speed is less than 1 m/s, the temperature difference of the battery pack will increase with an increase in the wind speed, and when the wind speed is greater than 2 m/s, the temperature difference will decrease with an increase in the wind speed. Chen *et al.* [13] compared the four methods of forced air cooling, fin cooling, direct liquid cooling, and indirect liquid cooling and determined that the power consumption of forced air cooling is greater under the same temperature rise of the battery, which is 2-3 times that of several other methods. Direct liquid cooling is generally performed via direct contact with a battery using an insulating fluid, such as a cooling oil, to exchange the heat via heat conduction. Hirano *et al.* [14] used a diele ctric liquid containing 99.5% C3F7OCH3 (a kind of hydrofluoroether) to directly cool the battery module. Their results showed that the battery's temperature can be controlled at 35±2.5 °C, even at a high discharge c-rate (20 C). However, high viscosity cooling oils result in higher pressure losses and the oil pump consumes more energy [15]. For indirect liquid cooling, the battery is not in direct contact with the liquid, and the heat of the battery is transferred to the cooling duct or the cold plate through heat conduction. Then, the heat of the cooling duct or the cold plate is taken away by the cooling liquid. Zhang *et al.* [16] designed a thermal management system with a staggered aluminum flat tube-wrapped battery. A flexible graphite sheet with a high thermal conductivity was inserted between the battery wall and the flat tube, which can increase the thermal conductivity between battery and the flat tube. The results show that this thermal management system can greatly improve the temperature uniformity of the battery pack and that the maximum temperature difference is reduced from 7 °C to 2 °C. Pradyumna Goli *et al.* [17] proposed a graphite-enhanced hybrid phase change material for use in lithium-ion battery thermal management systems. Four different percentages of the mixed phase change materials were prepared from 1% to 20%, depending on the percentage of the graphene content. The experimental results indicated that the temperature of the mixed material with 20% graphene is lower than that of the other groups. Tran *et al.* [18] proposed a cooling scheme that combined flat heat pipes with natural and forced convection for the thermal management of lithium-ion batteries in hybrid vehicles. The cooling performances of the heat pipe under different heat pipe inclination angles and fin inclination angles were analyzed. Tested under different conditions, the temperature was kept below 50 °C. Hamut *et al.* [19] designed a secondary loop cooling scheme in combination with the air conditioning system, where the refrigerant is R134a. The heat of the battery is transferred to the coolant through the cooling duct, and then, the coolant is exchanged heat with the refrigerant through the chiller. A second law analysis of the secondary loop cooling scheme was performed at high ambient temperatures. It was determined that the energetic COP (coefficient of performance) and exergetic COP ranges were 1.8–2.4 and 0.26–0.39, respectively. Shen and Gao [20] proposed a refrigerant-based battery thermal management system for electric vehicle. The energy efficiency of the system was analyzed under high temperature and extreme operating conditions. The PID controller was used to control the temperature of battery and cabin The results show that the refrigerant-based thermal management system can effectively control the temperature rise of the system, and the temperature difference is about 3 °C. However, the proper temperature of battery is a range, not a definite point. It is not necessary to control the battery temperature near a very low point. This approach may increase the energy consumption of the cooling system.

In terms of a cooling system control strategy, the rule-based control methods are currently widely adopted, such as the logic threshold method [21], [22] and the temperature detector method [23]. Wei [24] divided the battery temperature into four temperature ranges: the lower limit of the temperature (20 °C), the passive cooling temperature (35 °C), the active cooling temperature (38 °C), and the upper temperature limit (40 °C). When the temperature reaches the active cooling temperature, the refrigerant circuit is turned on, and the battery is cooled by the air conditioning system. It was determined that the temperature can be controlled within an appropriate range. The rule-based control strategy is easy to implement, simple to control, and effective. However, this traditional rule-based control strategy does not have an optimized theoretical basis and cannot optimize the problems we care about, such as system energy consumption, battery aging losses, and so on. Wang and Lukic [25] optimized the three typical powertrains of the Toyota Prius HEV with a dynamic programming (DP) algorithm with fuel economy and battery health (SOH) as the cost function. The simulation results show that there is a 30% potential improvement in overall cost. Then real-time control algorithm was developed based on DP optimization results, and the overall cost was improved by 27%, which is very close to the optimal result. Li *et al.* [26] proposed a multi-objective optimization approach to energy management strategies for extended-range electric vehicles to match the fuel economy and the battery health (SOH). The multi-objective optimization problem is solved by the DP algorithm. In addition, there are many scholars using the optimal control strategy algorithm used in electric vehicles, such as dynamic programming [27], [28], pontryagin's maximum principle [29], nonlinear programming [30], the model prediction [31]. Dynamic programming (DP) is a global optimization method for segmentation decision making, where the optimal decision in each time step is obtained. It can achieve global optimization. However, as the number of state variables and control variables increases, and the time step size increases, the amount of computation increases exponentially, resulting in a "dimension disaster", thus limiting its application in complex systems. A genetic algorithm can realize the group competition, natural selection, genetics and mutation based on biological evolution through computer simulation. This is a global optimization

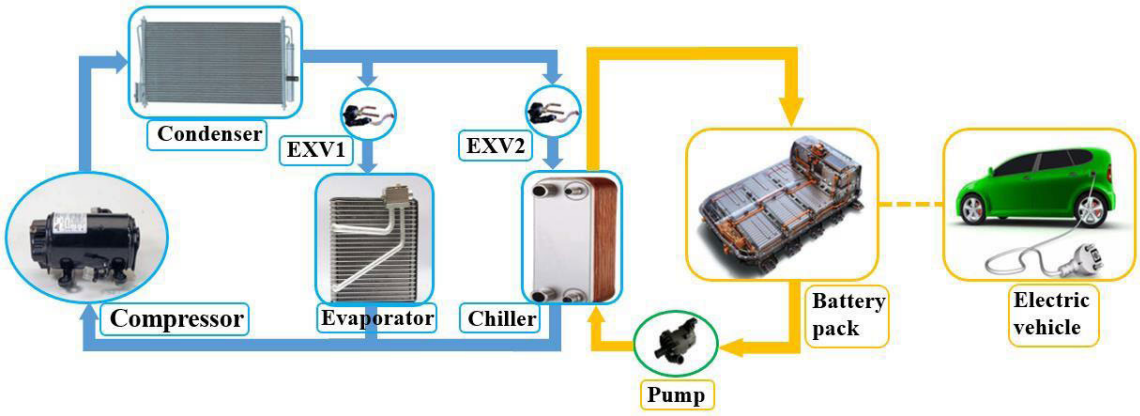

FIGURE 1. Schematic diagram of the secondary loop cooling system.

algorithm and has a wide range of applications in combinatorial optimization [32]. Therefore, this paper will adopt the genetic algorithm to optimize the system's control strategy.

In short, there are still some shortcomings in the current research on battery thermal management systems. First, the poor cooling performance of the air-cooling system, the high cost of the heat pipe cooling system, and the phase change material cooling system is complex and difficult to control. Second, for the current research on liquid cooling systems, usually only the temperature of the battery is considered, and the energy consumption of the system is not. Third, current studies on the battery thermal management system have barely considered the aging losses of the battery. Finally, there are few studies which considered the coupling relationship between the energy consumption of cooling system and the aging losses of the battery.

Motivated by the aforementioned research defects, there are four main contributions proposed in this paper. First, based on a secondary loop cooling system, the compressor speed as a decision variable and a phased control strategy for adjusting the compressor speed according to the battery temperature interval is proposed. Second, based on the first-order RC equivalent circuit model, a thermoelectric aging coupling model is established, which fully considers the coupling relationships among the SOC, the temperature distribution, and the heat generation, as well as the effect of the electrical parameters and the temperature on the aging losses of the battery. Third, both the aging losses of battery and the energy consumption of compressor are as the optimization goals, the genetic algorithm is adopted to solve the multi-objective optimization model. Finally, the Pareto Frontier of the energy consumption and the aging losses is established, under different weight coefficients. A balance control strategy is obtained, which can maximize the overall benefits.

The remainder of this paper is structured as follows. Section II introduces the mathematical model of the battery and the air conditioning system model. The validation of the secondary loop cooling system is in section III. Section IV describes the phased control strategy, and the multi-objective optimization model. The results and analysis of the phased control strategy are presented in section V. The final section describes the main conclusions and future outlook.

II. MATHEMATICAL MODEL

The secondary loop cooling system designed in this paper is shown in Fig. 1. It consists of a compressor, condenser, evaporator, chiller, two electronic expansion valves (EXV), and a battery pack cooling module. Based on the traditional air conditioning system, the chiller of the battery circuit is connected in parallel with the cabin evaporator to form a dual evaporator thermal management system. The high-temperature and high-pressure superheated gaseous refrigerant compressed by the compressor first exchanges heat with the outside air through a condenser to form a low-temperature and high-pressure subcooled liquid refrigerant. The liquid refrigerant coming out from the condenser is divided into two branches, which respectively pass through the electronic expansion valves of the respective branches. After adiabatic expansion, the refrigerant becomes a low-temperature and low-pressure liquid, and then enters the chiller and or the cabin evaporator to exchange heat with the object to be cooled (coolant or air). After the heat exchange in the chiller and the cabin evaporator, the refrigerant becomes low-temperature and low-pressure gas, and then merges at the compressor inlet and enters the cylinder to circulate again.

A. MODEL OF THE BATTERY

1) ELECTRIC MODEL OF THE BATTERY

Common battery models include neural network models, electrochemical models, equivalent circuit models, etc. The equivalent circuit model can well describe the electrical and thermal characteristics of the cell. The first-order RC equivalent circuit model [33] used in this paper is shown in Fig. 2. It consists of a constant voltage source U_{oc}, an ohmic internal resistance R_o, a polarization internal resistance capacitance R_p and a polarization capacitor C_p, U_t is the terminal voltage. Their calculation relationship is as shown in (1)-(4).

The terminal voltage U_t, the voltage U_o across the ohmic internal resistance, and the voltage U_p across the polarization

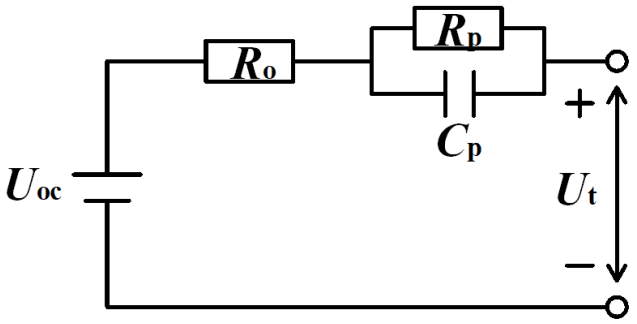

FIGURE 2. First-order equivalent circuit model.

internal resistance are calculated as (1)-(3):

$$U_t(t) = U_{oc}(\mathrm{SOC}) + U_o(t) + U_p(t) \tag{1}$$

$$U_o(t) = I(t)R_o(T, \mathrm{SOC}) \tag{2}$$

$$U_p(t) = U_p(0)\exp^{-t/R_1(T,\mathrm{SOC})C_1(T,\mathrm{SOC})} + I(t)R_0(T,\mathrm{SOC})\left(1-\exp^{-t/R_1(T,\mathrm{SOC})C_1(T,\mathrm{SOC})}\right) \tag{3}$$

The SOC (state of charge) can be obtained by the following equation (C_{bat} is the cell capacity):

$$\mathrm{SOC}(t) = 100\int_{t_0}^{t}\frac{I}{3600C_{bat}}dt \tag{4}$$

In (1)-(4), I represents current, t represents time and T represents the temperature of the battery. The above physical quantities are functions related to the battery temperature T and the battery SOC, and the functional relationship can be obtained by nonlinear regression of the test data of the battery.

2) THERMAL MODEL OF THE BATTERY

Xie *et al.* [34] have shown that the total heat generation Q_0 includes the irreversible heat generated by the ohmic internal resistance and the polarization internal resistance, as well as the reversible heat of reaction caused by the entropy increase of electrochemical reaction itself, the total heat generation is calculated as:

$$Q_0 = I^2(R_o + R_p) + IT\left(\frac{dU_{oc}}{dT}\right)_{soc} \tag{5}$$

where Q_0 is the total heat generated inside the battery, I is the current, T is the temperature of the battery, R_o, R_p are the ohmic internal resistance and the polarization internal resistance of the battery, respectively. dU_{oc}/dT is the entropy change, and its value can be calculated according to the test data of temperature rise and the open circuit voltage changes under different SOC.

During the driving process, the heat generated by the battery first transfers to the cooling duct through the heat conduction form, and then, the coolant and the cooling duct exchange heat in the form of convection, the temperature of the coolant rises. And then, the coolant exchanges heat with the refrigerant in the chiller, the temperature of the coolant is lowered. The low temperature coolant from the chiller again removes the heat from the cooling duct through the pump circulation. For complex systems, the research focus is on the interaction of the various components in the system, focusing on the entire system, not the internal mechanisms of the components. The lumped parameter method can do this well done and can greatly simplify the amount of calculation. So, in this paper, the lumped parameter method is adopted to model the heat exchange between the battery and the outside, and the battery is regarded as a uniform object, the established heat transfer relationship is shown in Fig. 3. And the relevant calculations are as follows:

$$\frac{dT}{dt} = \frac{Q_0 - Q_1}{mc_{p,bat}} \tag{6}$$

$$Q_1 = \frac{A_1(T - T_{duct})}{\lambda_{bat}/\delta_{bat} + \lambda_{duct}/\delta_{duct}} \tag{7}$$

$$Q_2 = hA_2(T_{duct} - T_{coolant}) \tag{8}$$

$$h = Nu\lambda_{coolant}/d_h \tag{9}$$

The laminar flow forced convective heat transfer correlation in-tube is [35]:

$$Nu = 1.86\left(\frac{RePr}{l/d_h}\right)^{1/3}(c_t)^{0.14} \tag{10}$$

The turbulent flow forced convective heat transfer correlation in-tube is [35]:

$$Nu = 0.023Re^{0.8}Pr^{0.4} \tag{11}$$

In (6)-(11), T, T_{duct}, and $T_{coolant}$ are the cell temperature, cooling duct temperature, and coolant temperature, respectively. Q_1 is the heat transfer rate between the cell and the cooling duct, Q_2 is the heat transfer rate between the cooling duct and the coolant, and A_1 and A_2 are the contact area between the cell and the cooling duct, and the heat exchange area of the coolant and the cooling duct, respectively. h is the convective heat transfer coefficient, and Nu, Re, Pr are the Nusselt number, the Reynolds number, and the Prandtl number, respectively. L is the length of the cooling duct, d_h is the hydraulic diameter of the cooling duct, and c_t is the temperature correction factor. λ_{bat}, λ_{duct}, and $\lambda_{coolant}$ are the thermal conductivities of the cell, cooling duct and coolant, respectively. λ_{bat} is the distances between the cell center point and the contact surface, λ_{duct} is the distances between the duct center point and the contact surface.

The heat transfer between the coolant and the refrigerant in the chiller can be calculated based on the flow rate and the boundary conditions of the fluid on both sides. The model of the chiller will be given in the air conditioning system and experimentally verified. Therefore, the temperature rise of the cell can be calculated from (5)-(11).

3) AGING LOSS MODEL OF THE BATTERY

When the battery is placed for a long time or cyclically used, the maximum capacity attenuation will inevitably occur, this

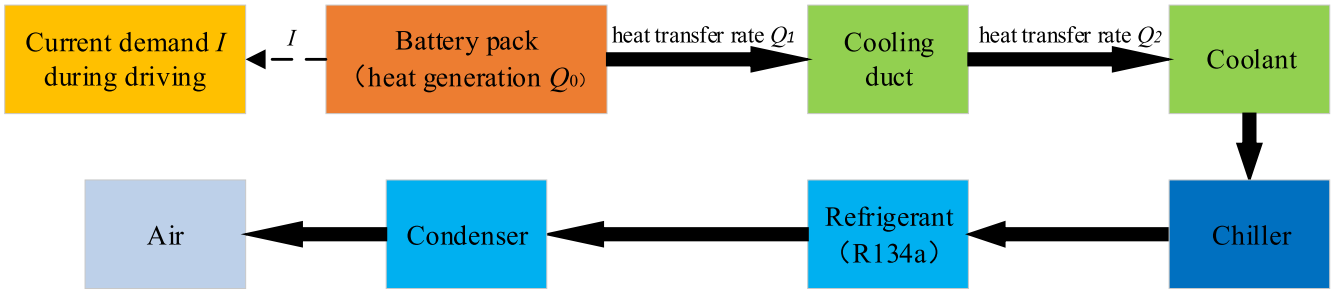

FIGURE 3. Schematic diagram of heat transfer relationship.

TABLE 1. Parameters of the empirical aging model.

B	Ea	α	z
130	18461	32	0.4

phenomenon is the aging losses of the battery. The working environment of the battery, the charging and discharging conditions, and the depth of discharge all affect the degree of attenuation of the maximum capacity of the battery. Wang *et al.* [36] conducted a large number of experiments to study the cycle life of a cell under different temperatures (from -30 °C to 60 °C), depths of discharge (from 10% to 90%) and discharge C-rates (from 0.5 C to 10 C). On this base, Petit *et al.* [37] calibrated and validated for a NCA/C Li-ion cell. The fitting formula for the aging losses of the cell is obtained based on the experimental results as follows:

$$Q_{\text{loss}} = B \cdot e^{\frac{-Ea+\alpha|I|}{RT}} (Ah)^z \tag{12}$$

where B is a pre exponential factor which depends on current I, Ea is an activation energy for cycle aging, α is a coefficient for aging acceleration due to current, R is the gas constant, T is the cell temperature (Kelvin), z is an exponent constant that should be around 0.5 for diffusion limited process, and Ah stands for Ah throughput, that is the amount of charge sent into the cell. The parameters used for these technologies are indicated in Table 1.

For a power battery, when the battery capacity losses reach 20%, the battery cycle life is generally considered to be exhausted. That is, when $Q_{\text{loss}} = 20\%$, the battery cycle life SOH (state of health) $= 0$. When the battery is new $Q_{\text{loss}} = 0$, which corresponds to $SOH = 1$. Therefore, the cycle life of the power battery is expressed as $SOH = 1 - Q_{\text{loss}}/20\%$, and the aging losses Q_{loss}' of the power battery can be expressed by (13):

$$Q'_{\text{loss}} = 1 - SOH = Q_{\text{loss}}/20\% \tag{13}$$

The aging losses calculation described above is for a cell, and the actual battery pack is composed of many single cells in series and parallel. In general, the cycle life of a battery pack is determined by the cell with the worst state. In this paper, the aging losses of the battery module with the worst state will be used as the aging losses of the entire battery pack.

The schematic diagram of the thermoelectric aging coupling model of the battery is shown in Fig. 4. The heat generation Q_0 calculated from the electrical parameters of the first-order RC equivalent circuit model is transferred to the thermal model, and the battery temperature calculated by the thermal model is fed back to the equivalent circuit model to calculate the impedance and capacitive reactance of the electrical model. The electrical parameters of the equivalent circuit model and the temperature of the thermal model are fed back to the aging model to calculate the aging losses of the battery.

B. MODEL OF AIR CONDITIONING SYSTEM

1) MODEL OF THE COMPRESSOR

The function of the compressor is to compress the low-temperature and low-pressure gaseous R134a refrigerant into high-temperature and high-pressure gas. The focus of this paper is on the overall system's simulation, not on the compressor's components. Therefore, in the modeling, it is based on three parameters that affect the performance of the compressor. The performance parameters affecting the compressor mainly include volumetric efficiency, isentropic efficiency and mechanical efficiency. The relevant calculation formula is as follows:

$$\eta_{\text{v}} = \frac{dm}{\rho_{\text{suc}} N disp} \tag{14}$$

$$\eta_{\text{is}} = \frac{h_{\text{dis}} - h_{\text{s}}}{h_{\text{d}} - h_{\text{s}}} \tag{15}$$

$$\eta_{\text{m}} = \frac{dm(h_{\text{d}} - h_{\text{s}})}{\tau N} \tag{16}$$

where η_{v}, η_{is}, η_{m} are volumetric efficiency, isentropic efficiency and mechanical efficiency respectively. dm is the mass flow rate, ρ_{suc} is the suction density, N is the compressor speed, $disp$ is the compressor displacement, h_{dis} is the isentropic discharge specific enthalpy, h_{d} is discharge specific enthalpy, h_{s} is the suction specific enthalpy, τ is the torque.

Therefore, the mass flow, suction enthalpy flow, exhaust enthalpy flow, and output torque are calculated as follows:

$$dm = \eta_{\text{v}} \rho_{\text{suc}} N disp \tag{17}$$

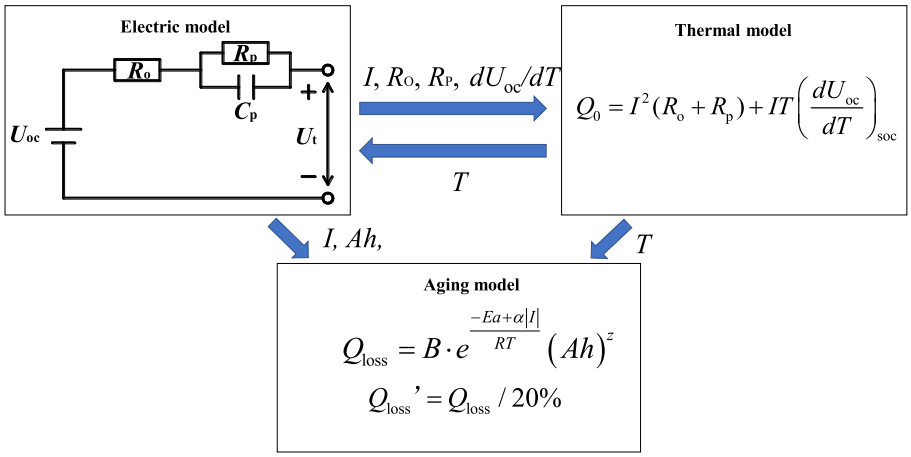

FIGURE 4. Thermoelectric aging coupling model.

$$h_1 = -dmh_s \tag{18}$$
$$h_2 = -h_1 + dm(h_{dis} - h_s)/\eta_{is} \tag{19}$$
$$\tau = \frac{dm - (h_{dis} - h_s)/\eta_{is}}{N\eta_m} \tag{20}$$

2) MODEL OF THE CONDENSER

The condenser is a tube-fin heat exchanger. Its role is to cool the high-temperature and high-pressure gaseous refrigerant from the compressor to a low-temperature and high-pressure liquid. The heat exchanger model established in this paper fully considers the internal heat transfer of refrigerant and the external heat transfer of moist air. The condenser model mainly includes three parts: the refrigerant side's heat transfer (internal flow), the geometry parameters of the microchannel and fins, and the moist air side's heat transfer (external flow). The microchannel are discretely divided into several module units, where each unit includes a resistive unit and a capacitive unit, as shown in Fig. 5.

In Fig. 5, *dh* represents the heat exchange and *t* represents the temperature. Resistive unit variables include *Re*, *Pr*, and *ff*, which represent the Reynolds number, Prandtl number, and friction factor, respectively. Capacitive unit variables include *dp* and *droh*, which represent changes in the pressure and density, respectively.

The internal heat exchange of the refrigerant, that is, the heat exchange between the refrigerant and the wall of the condenser microchannel, is calculated by (21).

$$\phi_{int} = h_{c,int}S_{int}(T_{ref} - T_{wall}) \tag{21}$$

The condensation process of the refrigerant in the condenser has a single-phase heat transfer and a two-phase heat transfer. Here, the convective heat transfer coefficient $h_{c,int}$, which is the calculation formula of the two-phase heat transfer, as shown in (22). For the single-phase heat transfer, refer to the literature [38].

$$h_{c,int} = h_{LO}\left[(1-x)^{0.8} + (3.8\frac{x^{0.76}(1-x)^{0.04}}{P_{red}^{0.38}})\right] \tag{22}$$

In (21)-(22), $h_{c,int}$ is the internal convective heat transfer coefficient, S_{int} is the heat exchange area, T_{ref} is the temperature of the refrigerant, T_{wall} is the temperature of the microchannel wall, h_{LO} is the convective heat transfer coefficient of the refrigerant's single-phase liquid heat exchange, P_{red} is the corresponding pressure drop, and x is the refrigerant gas mass fraction.

For the heat transfer of the outer surface of the condenser microchannel and the moist air, the calculation formula is as follows:

$$\phi_{ext} = h_{c,ext}S_{ext}(T_{mo} - T_{wall}) \tag{23}$$
$$h_{c,ext} = Nu\lambda_{mo}/(d_h) \tag{24}$$
$$Nu = aRe^bPr^c \tag{25}$$

where $h_{c,ext}$ is the external heat transfer coefficient, S_{ext} is the external heat exchange area, and T_{mo} and T_{wall} are temperatures of the moist air and the wall, respectively. λ_{mo} is the thermal conductivity of moist air, and d_h is the moist air side's hydraulic diameter. *Nu* is calculated by (25), and *Re* and *Pr* are the Reynolds number and Prandtl number, respectively, which are related to the moist air flow state. The coefficients *a*, *b*, and *c* are verified by experimental and simulation data.

The heat exchange between the microchannel wall and the fins depends on the internal and external heat exchange for the unit. The wall temperature are state variables and can be computed from the time derivatives as follows:

$$\frac{dT_{wall}}{dt} = \frac{\phi_{int} + \phi_{ext}}{mc_p} \tag{26}$$

where m is the mass of the calculated unit, and c_p is the specific heat of the wall material.

3) MODEL OF THE EVAPORATOR

The evaporator is also a tube-fin heat exchanger. The low-temperature condensed liquid refrigerant passes through the evaporator, exchanges heat with the outside moist air, vaporizes and absorbs heat, and achieves the cooling effect. The

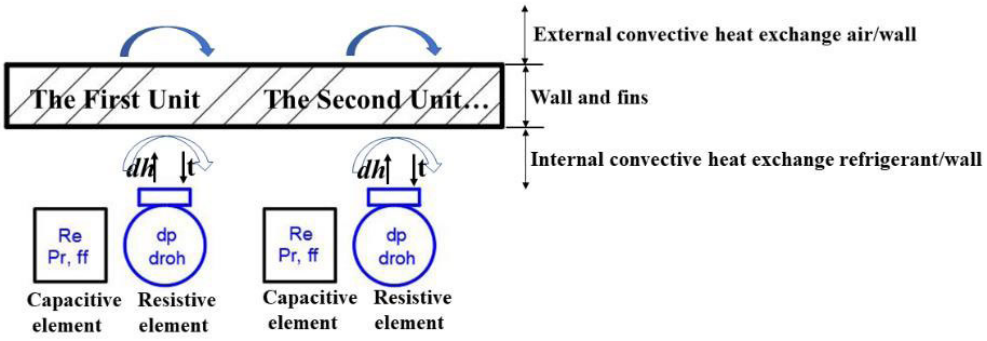

FIGURE 5. Schematic diagram of the heat exchange unit of the condenser.

TABLE 2. Parameters of cell.

Parameters	Value
Cell capacity (Ah)	3.4
Cell voltage (V)	3.6
Charge cut-off voltage (V)	4.2
Density (kg/m^3)	2776.3
Specific heat (J/k/kg)	1075.9

heat exchanger model of the evaporator fully considers the internal heat transfer of refrigerant and the external heat transfer of moist air. It is similar to the condenser. The main parameters include the internal heat transfer between the refrigerant and the microchannel wall, the external heat transfer between the moist air and the outside wall, and the geometric parameters of the microchannel and the fins. The modeling process is similar to the condenser and will not be described here.

4) MODEL OF THE CHILLER

The chiller is a plate heat exchanger with a coolant and refrigerant on both sides. The role of chiller is to transfer the cooling capacity of the air conditioning system to the coolant circuit. In chiller, the refrigerant absorbs the heat of the coolant to reduce the temperature of the coolant, thereby cooling the battery. The main parameters include the geometry parameters of chiller, the heat transfer between the refrigerant and the plate wall, and the heat transfer between the coolant and the plate wall. The modeling process is similar to the condenser.

The heat transfer calculation of the refrigerant and the wall is similar to the internal flow heat transfer between the refrigerant and the wall of the condenser model, so it will not be described here. The difference is the heat transfer between the coolant and the wall. The heat transfer between the coolant and the wall is calculated as follows:

$$\phi_{\mathrm{THH}} = h_{\mathrm{THH}} \Delta T_{\mathrm{THH}} \tag{27}$$

$$h_{\mathrm{THH}} = h_{\mathrm{conv}} k_{\mathrm{THH}} \tag{28}$$

$$h_{\mathrm{conv}} = Nu \lambda_{\mathrm{coolant}} / d_{\mathrm{h}} \tag{29}$$

$$Nu = a Re^{b} Pr^{c} \tag{30}$$

where h_{conv} is the heat transfer coefficient calculated by Nu, k_{THH} is the heat transfer gain, h_{THH} is the corrected heat exchange coefficient on the coolant side, and ΔT_{THH} is the temperature difference between the coolant and the wall. The corrected coefficients a, b, and c are verified based on the experimental data and the simulation data.

The wall temperature T_{p} depends on the heat exchange of the fluid on both sides of the component. As state variables, they can be computed from the time derivatives as follows:

$$\frac{dT_{\mathrm{p}}}{dt} = \frac{\phi_{\mathrm{TPF}} + \phi_{\mathrm{THH}}}{m c_{\mathrm{p,p}}} \tag{31}$$

where ϕ_{TPF} and ϕ_{THH} are the heat transfer rates between the refrigerant side and the coolant side and the wall, respectively, m is the mass of the calculated unit, and $c_{\mathrm{p,p}}$ is the constant pressure specific heat of the wall material.

5) MODEL OF THE EXV

The function of the electronic expansion valve is to adjust the valve opening degree by collecting the superheat signal of the evaporator outlet. The electronic expansion valve model used in this paper is a variable aperture throttle model, and the valve opening is determined according to the input signal. The cross-sectional area, hydraulic diameter and mass flow rate are calculated as follows:

$$S_{\mathrm{carea}} = sig \times A_{\mathrm{max}} \tag{32}$$

$$d_{\mathrm{h}} = sig \times d_{\mathrm{max}} \tag{33}$$

$$dm = C_{\mathrm{q}} S_{\mathrm{carea}} \sqrt{2 \Delta P \rho_{\mathrm{up}} / k_{\mathrm{dp}}} \tag{34}$$

where sig is the valve opening signal, A_{max} and d_{max} are the maximum cross-sectional area and diameter of the throttle valve, respectively, and S_{carea} and d_{h} are the cross-sectional area and hydraulic diameter of the refrigerant currently flowing, respectively. dm is the mass flow rate of the refrigerant, ΔP is the pressure difference of the import and export, ρ_{up} and k_{dp} are the density of the refrigerant at the upstream and the pressure loss gain, respectively. Finally, C_{q} is the flow coefficient [39].

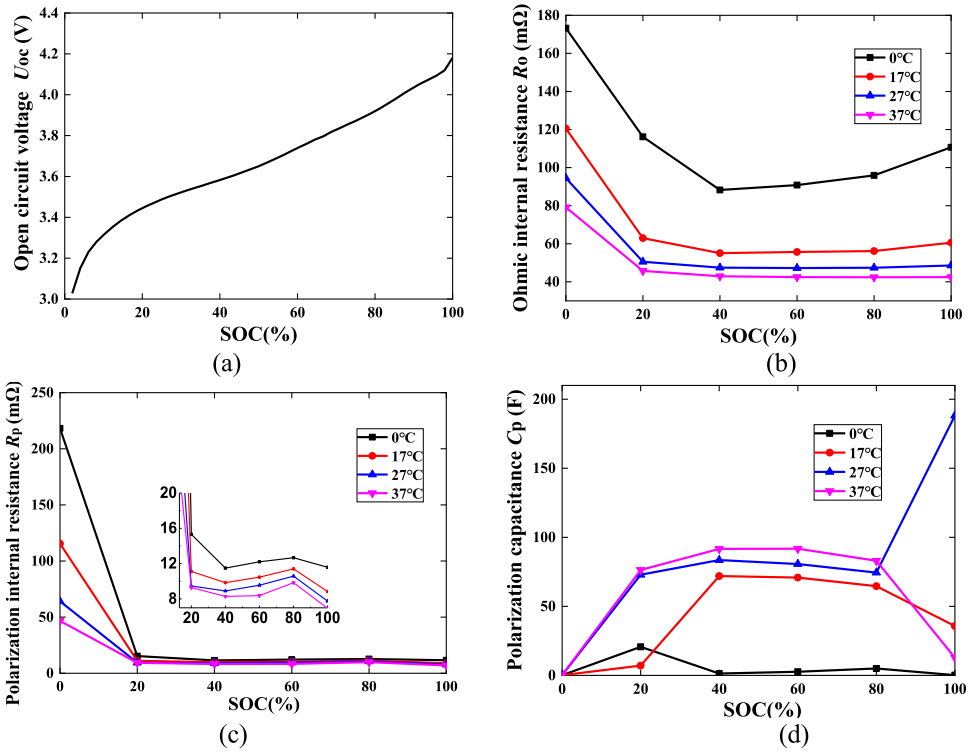

FIGURE 6. Electrical parameters under different temperatures and SOC: (a) open circuit voltage U_{oc}, (b) ohmic internal resistance R_o, (c) polarization internal resistance R_p, (d) polarization capacitance C_p.

III. VALIDATION OF THE SECONDARY LOOP COOLING SYSTEM

Considering the complexity of the whole system, only carried out experimental verification on important components of the cooling system, only the cell and air-conditioning systems were experimentally verified for simulation.

A. VALIDATION OF THE BATTERY MODEL

The battery used in this paper is NCA (nickel-cobalt-aluminum) ternary lithium battery. The model is 18650B, and the battery parameters are shown in Table 2. In this paper, the battery model is a first-order RC equivalent circuit model. The main parameters include open circuit voltage U_{oc}, ohmic internal resistance R_o, polarization internal resistance R_p, and polarization capacitance C_p. The U_{oc} can be measured directly under different *SOC*. The HPPC (Hybrid Pulse Power Characteristic) experimental method can be used to measure the internal resistance characteristics of the battery, and then the value of the polarization capacitor can be calculated according to (3). The experimentally measured parameters are shown in Fig. 6.

The thermoelectric model of the battery was verified. In the experiment, the battery was placed in an adjustable charging tank, and the tank was placed in the thermostat (CK-150G, Dongguan Qinzhuo Environmental Testing Equipment Co., Ltd). The temperature range of the thermostat is from −20 °C to 150 °C, and its temperature departure is ±0.5 °C. The temperature of the thermostat was set to 27 °C, a K-type thermocouple was placed on the surface of the battery, and the battery temperature was measured using the Agilent 34972A. A Neware BTS4000 battery testing system was applied to measure the current and terminal voltage, and its measured accuracy with 0.01%. The battery was first charged by constant current of 1 C, charged to a cut-off voltage of 4.2 V, and then charged by constant voltage. The experimental equipment is shown in Fig. 7.

During the charging process, the comparison between the experimental results and the simulation results of the battery voltage and temperature with the charging time is shown in Fig. 8. It can be seen that the overall trends of experimental and simulation are similar. The maximum relative error of voltage between experimental and simulation is 1.00 %, and the maximum relative error of temperature is 2.53 %, which are acceptable.

B. VALIDATION OF AIR CONDITIONING SYSTEM MODEL

The electric compressor and heat exchanger of the air-conditioning system were experimentally verified. For electric compressor, experiments were performed at different pressure ratios (exhaust pressure ratio to suction pressure) and speeds. The volumetric efficiency and isentropic efficiency of the compressor were tested experimentally. The results are shown in Fig. 9. The mechanical efficiency of the compressor is generally 0.9.

For the three heat exchangers, the experimental conditions of the heat exchanger are shown in Table 3. The calibration of

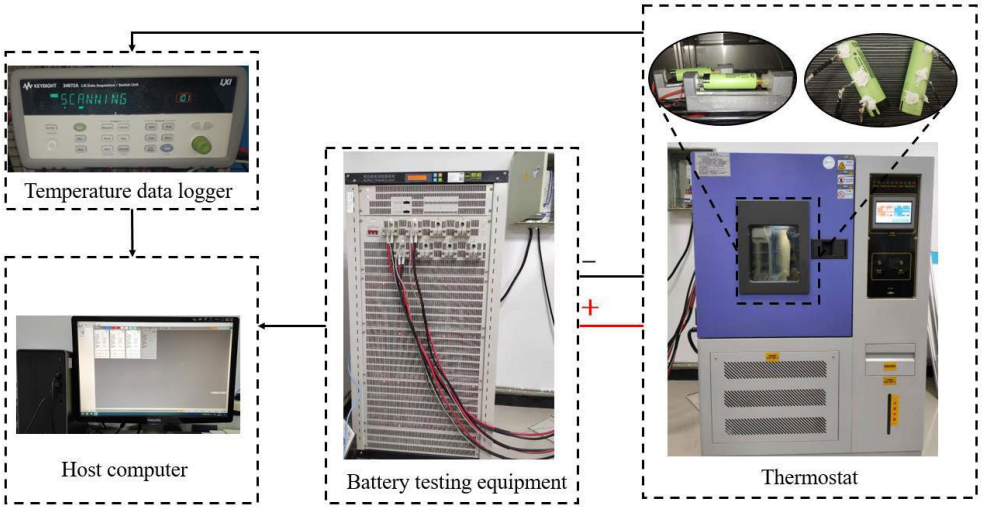

FIGURE 7. Sketch of experiment platform.

the heat exchanger model is to correct the three coefficients a, b, and c in (25) and (30), so that the relative errors between the experimental results and simulated results are minimized. The picture of the experimental validation is shown in Figure 10.

The comparison of the experimental results and simulation results of the calibrated condenser, evaporator, and chiller are shown in Fig. 11. The maximum relative errors are 2.82%, 0.65%, and 3.26%, respectively, which are acceptable.

IV. MULTI-OBJECTIVE OPTIMIZATION MODEL AND CONTROL STRATEGY

A. MULTI-OBJECEIVE OPTIMIZATION MODEL

Both The energy consumption of the compressor and the aging losses of the battery as optimization goals, which constitute a multi-objective optimization model.

The power of the compressor is denoted by P and the energy consumption is denoted by W. The power P of the compressor can be calculated by the enthalpy difference of the refrigerant inlet and outlet of the compressor, and the energy consumption W is calculated by integrating the power P in the corresponding working time.

$$P = h_2 - h_1 \tag{35}$$

$$W = \int Pdt \tag{36}$$

where h_1 represents the compressor refrigerant inlet enthalpy and h_2 represents the compressor refrigerant outlet enthalpy.

The aging loss model for batteries has been given in Section II, and the battery aging losses are expressed as Q_{loss}', and it can be calculated by (12)-(13).

Therefore, the multi-objective optimization model can be expressed as:

$$J = \min f = \beta \frac{W}{W_{\max}} + (1-\beta) Q'_{\text{loss}},$$

$$\text{s. t.} 20°\text{C} \le T_{\max} \le 40°\text{C}. \tag{37}$$

where f is the sum of two optimization goals under certain weighting coefficient, β represents the weighting coefficient of the compressor energy consumption, $W_{\max}$ represents the energy consumption at the maximum compressor speed, in order to make both optimization goals between 0-1, $W/W_{\max}$ is used to represent the optimization goal of energy consumption, and Q_{loss}' represent the optimization goal of the aging losses of the battery. $T_{\max}$ represents the maximum temperature of the battery, it was constrained between 20 °C and 40 °C.

B. PHASED CONTROL STRATEGY AND OPTIMIZATION

The phased control strategy proposed in this paper is based on the temperature of the battery. The decision variable of the simulation system, that is, the compressor speed n, is determined according to the current battery temperature value T. Considering the performance of the control and optimization, the smaller the temperature interval, the better the performance may be. However, as the number of temperature intervals increases, the amount of calculation will increase greatly. In this paper, the battery temperature interval is divided into five, that is, $T \le T_1$, $T_1 < T \le T_2$, $T_2 < T \le T_3$, $T_3 < T \le T_4$, and $T_4 < T \le T_5$. Their corresponding decisions are the compressor speeds n_i(i=1, 2, 3, …, 5). During simulation, when the battery temperature value meets one of the above temperature ranges, a certain control is applied, that is, a certain speed signal n_i is inputted. Then, the genetic algorithm is adopted to optimize the n_i value. So, it is worth mentioning that each decision variable n_i is optimized by the genetic algorithm under a certain control strategy.

The essence of genetic algorithm is to evolve from generation to generation according to the principle of survival of the fittest through group search technology, and finally get

TABLE 3. Experimental conditions of heat exchangers.

Heat exchanger	Experimental conditions
Condenser	Air side: inlet air temperature 35 °C, air relative humidity 40%, wind speeds are 1.2 m/s, 2.5 m/s, 3.5 m/s, 4.5 m/s, 6 m/s respectively Refrigerant side: condensing pressure 16.81 barA, refrigerant inlet specific enthalpy 274.85 KJ/Kg, subcooling degree 4.2 °C
Evaporator	Air side: inlet air temperature 27 °C, air relative humidity 50%, air volume flow rate is 300.0 m3/h, 400.0 m3/h, 500.0 m3/h respectively Refrigerant side: evaporation pressure 2.96 barA, refrigerant inlet specific enthalpy 458.9 KJ/Kg, refrigerant mass flow rate is 100.1 Kg/h, 126.9 Kg/h, 149.6 Kg/h respectively
Chiller	Coolant side: inlet temperature 25 °C, volume flow rate is 8 L/min, 10 L/min, 12 L/min, 15 L/min respectively Refrigerant side: refrigerant inlet specific enthalpy 271.6 KJ / Kg, refrigerant outlet pressure 4.013 barA, refrigerant mass flow rate is 56.4 Kg/h, 71.6 Kg/h, 78.3 Kg/h, 86.4 Kg/h respectively

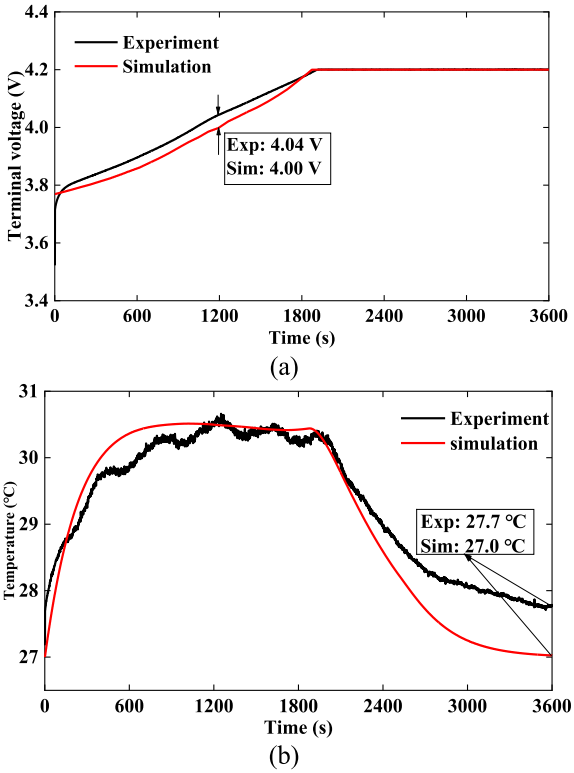

FIGURE 8. Battery thermoelectric model verification: (a) terminal voltage, (b) temperature.

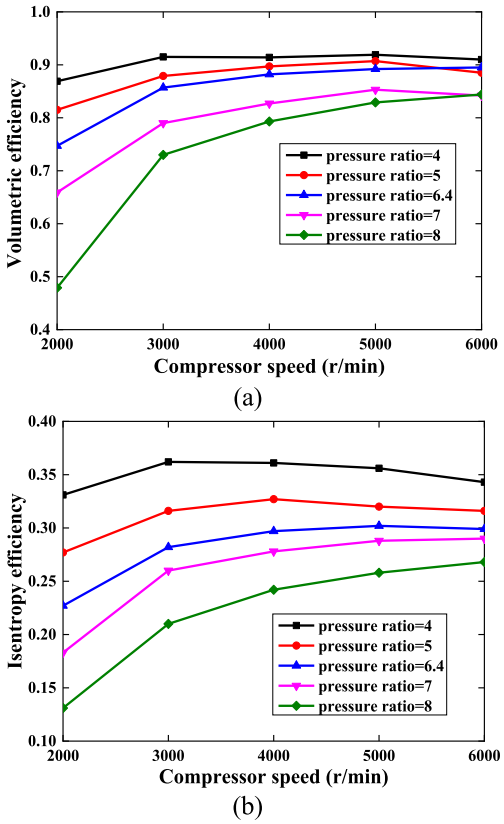

FIGURE 9. Performance parameters of the compressor: (a) volume efficiency, (b) isentropic efficiency.

the optimal solution or quasi-optimal solution. In this paper, the genetic algorithm is used to optimize the abovementioned phased control strategy, that is, to optimize the decision variable n_i(i=1, 2, 3, …, 5). The number of populations of the genetic algorithm is 50, that is, 50 sets of n_i (i=1, 2, 3, …, 5) values are randomly given at the time of initialization, and the maximum number of iterations is 1620 times. To ensure the full evolution of the population and large-scale optimization exploration, the regeneration rate is set to 0.8, the mutation probability is set to 0.1, and the mutation amplitude is set to 0.8. The schematic diagram of the phased control strategy is shown in Fig. 12.

V. RESULTS AND DISCUSSION

The battery pack's design is given in reference [40]. The battery capacity of electric vehicles is generally 50∼100 Ah, and the discharge voltage is generally approximately 350 V. The battery pack designed in this paper is divided into 5 modules

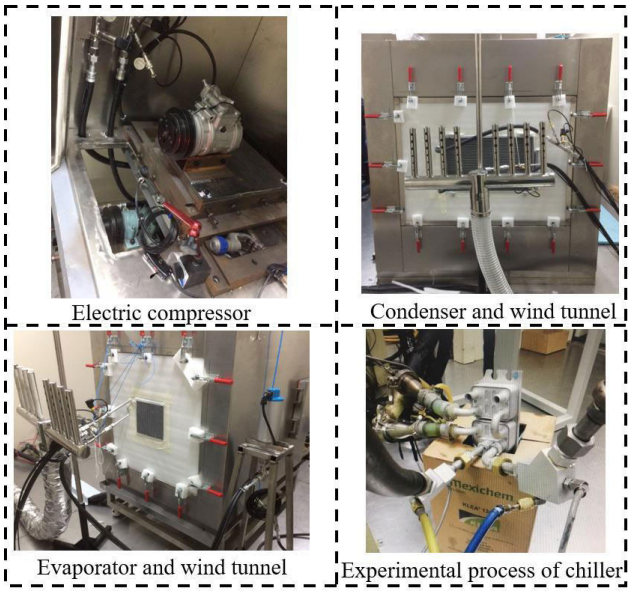

FIGURE 10. The experimental validation of heat exchangers.

in series. Each module consists of 3000 cells connected in 20 series and 15 parallel. The capacity of the battery pack is 51 Ah and the voltage is 360 V.

In order to test the battery temperature control effect of the secondary loop cooling system and the optimization effect of the control strategy, a higher ambient temperature of 30 °C and an extreme operating condition of 3 consecutive US06 cycles are selected. The initial temperature of the battery is the same as the ambient temperature is 30 °C. It is worth mentioning that the research object and control strategy are for battery packs, so the temperature control of the cabin is not considered. The simulation conditions are shown in table 4, and the driving cycle conditions are shown in Fig. 13. In the following simulation analysis, T_H represents the temperature of the battery module with the highest temperature in battery pack, and ΔT represents the temperature difference between modules in battery pack.

A. EFFECT OF THE COOLANT FLOW RATE AND THE COMPRESSOR

The two important evaluation indexes of the battery thermal management system are the maximum temperature and temperature uniformity of the battery pack. In the secondary loop cooling system, the factors affecting the maximum temperature $(T_H)_{max}$ and the maximum temperature difference $(\Delta T)_{max}$ are mainly the coolant flow rate of the coolant circuit and the compressor speed of the refrigerant circuit.

The effects of the coolant flow rate on the cooling performance of the cooling system were analyzed by simulation, under the conditions of the compressor speeds of 1000, 3000 and 5000 r/min. Fig. 14 shows the $(T_H)_{max}$ and $(\Delta T)_{max}$ throughout the simulation under different coolant flow rates. Fig. 14 (a) shows the change of $(T_H)_{max}$ with different coolant

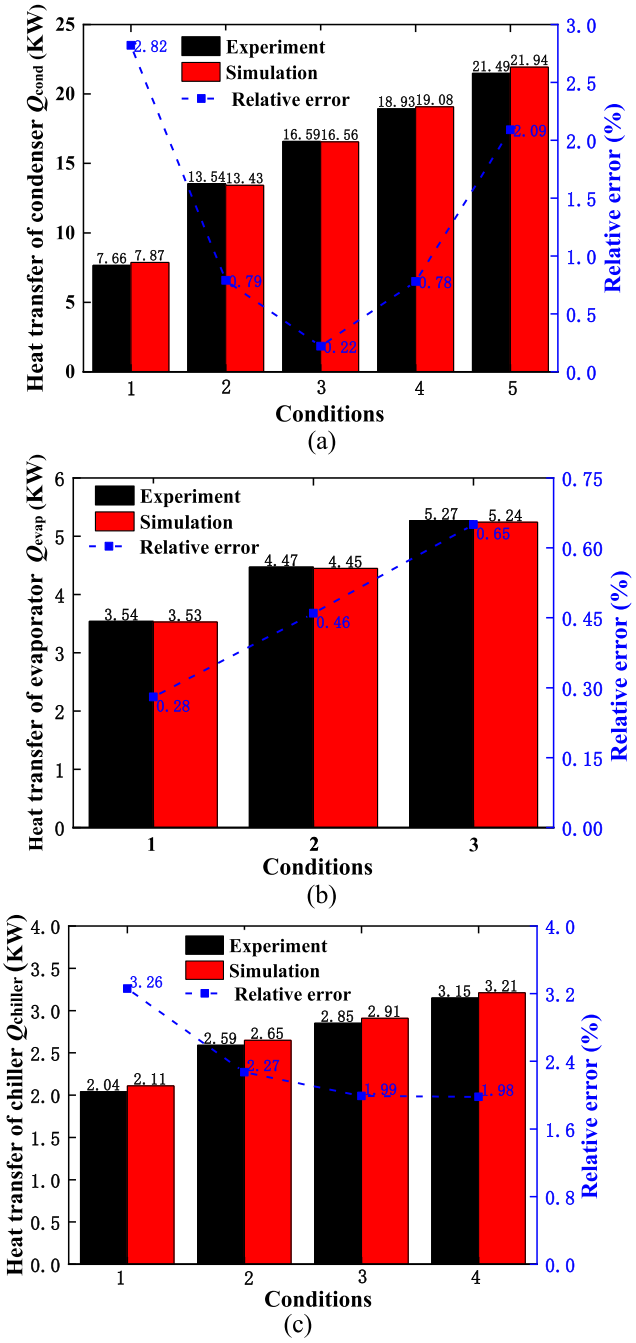

FIGURE 11. The Comparison of experimental results and simulation results: (a) heat transfer of condenser, (b) heat transfer of evaporator, (c) heat transfer of chiller.

flow rates at a certain compressor speed, $(T_H)_{max}$ decreases with increasing coolant flow rate. What's more, the larger the compressor speed, the more obvious the declining trend of the $(T_H)_{max}$. However, when the compressor speed is constant, the $(T_H)_{max}$ will not keep falling and will reach a minimum value as the coolant flow rate increases. Fig. 14 (b) shows the change of the $(\Delta T)_{max}$ with different coolant flow rates at a certain compressor speed. Under the condition that the compressor speed is constant, the downward trend is very

TABLE 4. Driving conditions.

Driving conditions	Ambient temperature	Duration
3 consecutive US06 cycles	30 °C	1800 s

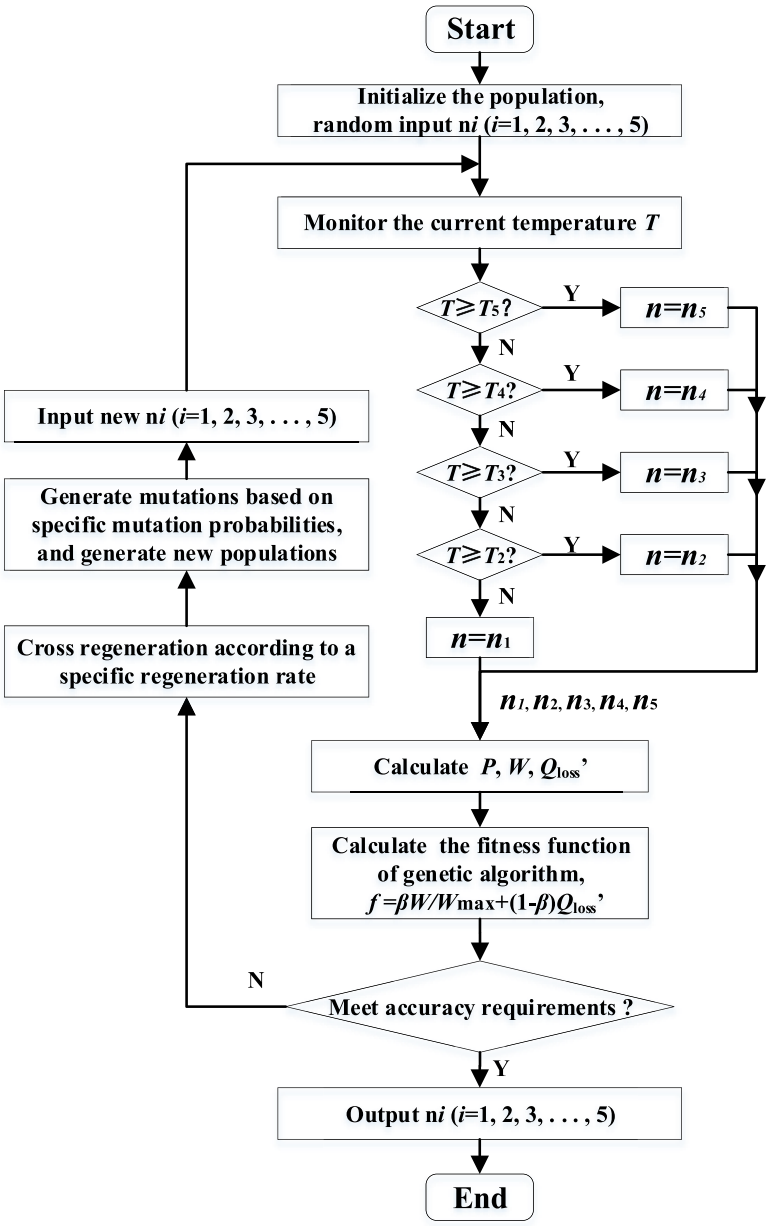

FIGURE 12. Schematic diagram of the phased control strategy.

significant with the increase of the coolant flow rate. Moreover, same trend as $(T_H)_{max}$, when the coolant flow rate is greater than 8 L/min, $(\Delta T)_{max}$ and $(T_H)_{max}$ are no longer reduced.

The influence of the compressor speed on the cooling performance of the battery pack was analyzed by simulation under the conditions of the coolant flow rate of 6, 8, and 10 L/min. Fig. 15 (a) shows the $(T_H)_{max}$ throughout the simulation under different compressor speeds. It can be seen that the $(T_H)_{max}$ decreases obviously with the increase of the compressor speed, which indicates that the compressor speed has a significant influence on $(T_H)_{max}$. Fig. 15 (b)

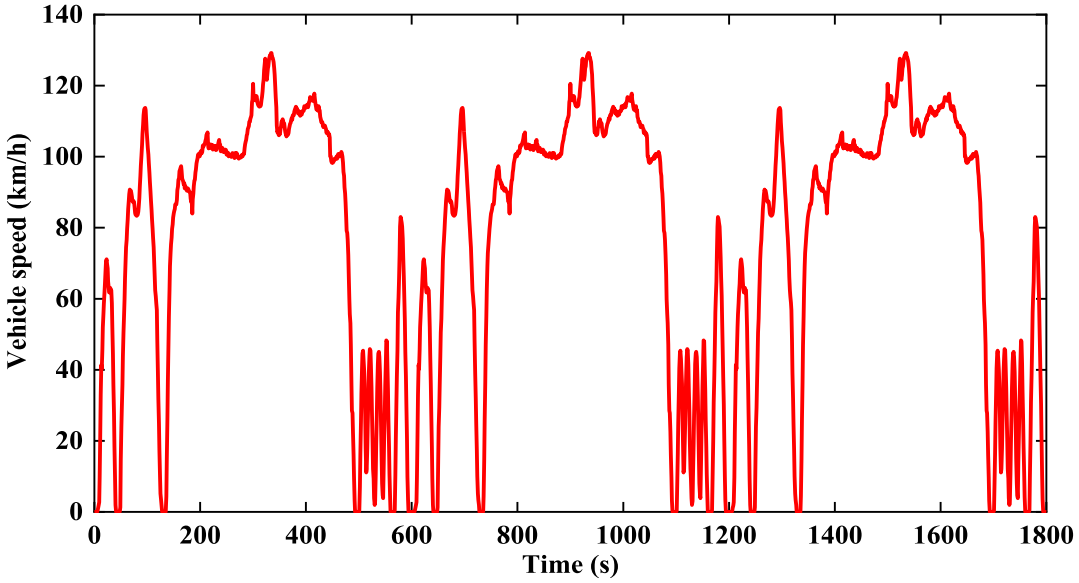

FIGURE 13. Driving cycle.

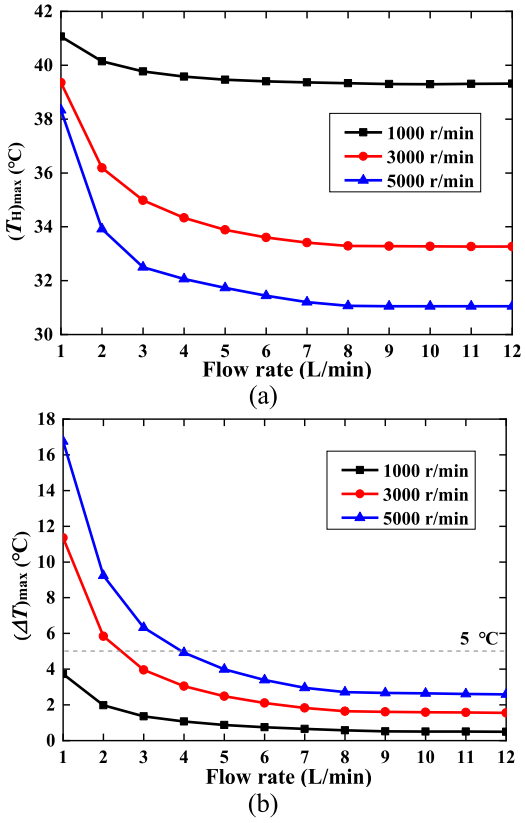

FIGURE 14. The variation of the $(T_H)_{max}$ and $(\Delta T)_{max}$ with different flow rate of coolant: (a) The maximum temperature of the battery module with the highest temperature in battery pack $(T_H)_{max}$, (b) the maximum temperature difference $(\Delta T)_{max}$.

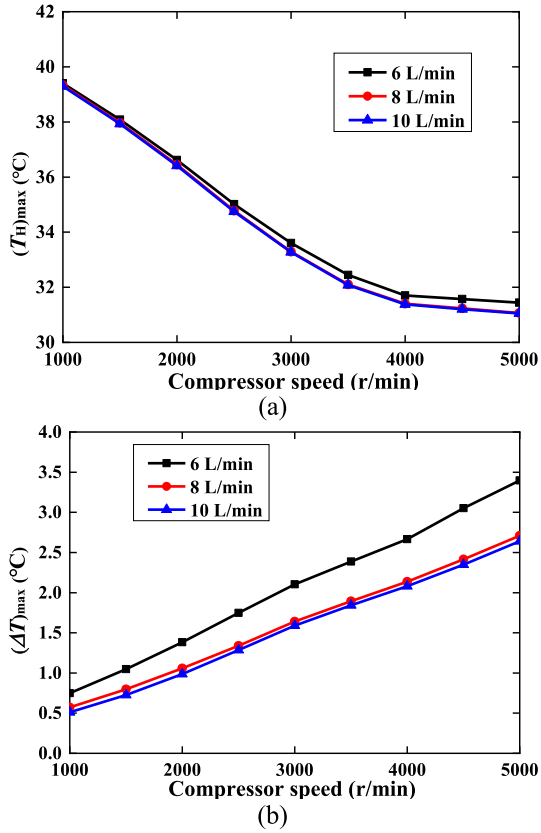

FIGURE 15. The variation of the $(T_H)_{max}$ and $(\Delta T)_{max}$ with different compressor speeds: (a) The maximum temperature of the battery module with the highest temperature in battery pack $(T_H)_{max}$, (b) the maximum temperature difference $(\Delta T)_{max}$.

shows the $(\Delta T)_{max}$ throughout the simulation under different compressor speeds. Unlike the change trend of $(T_H)_{max}$, the $(\Delta T)_{max}$ increase significantly as the compressor speed increases. The larger the compressor speed, the larger the cooling capacity of the air conditioning system, and the larger

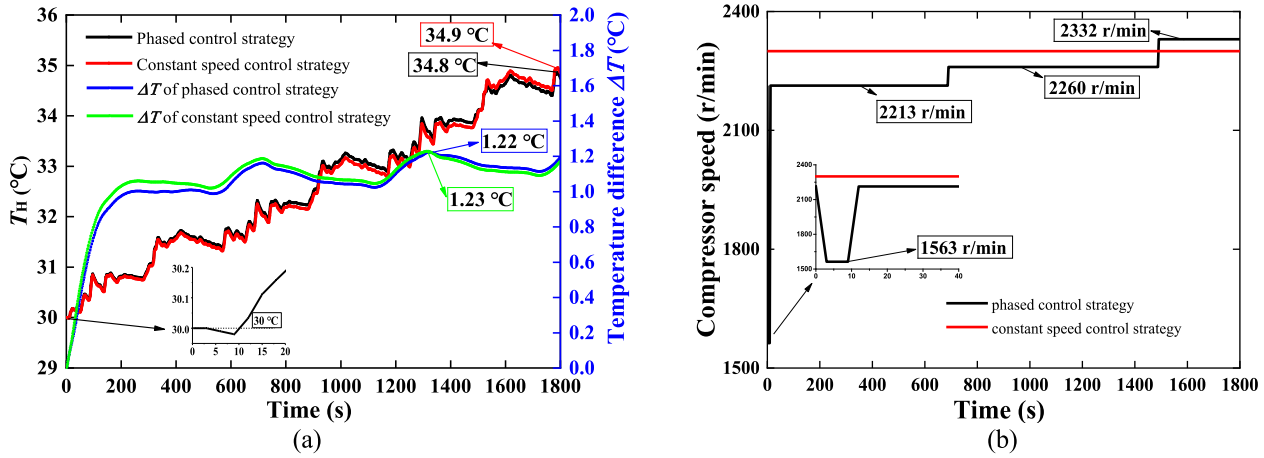

FIGURE 16. The comparison between the phased control strategy and the constant speed control strategy: (a) The temperature (T_H) of the battery module with the highest temperature in battery pack and the temperature difference ΔT, (b) compressor speed.

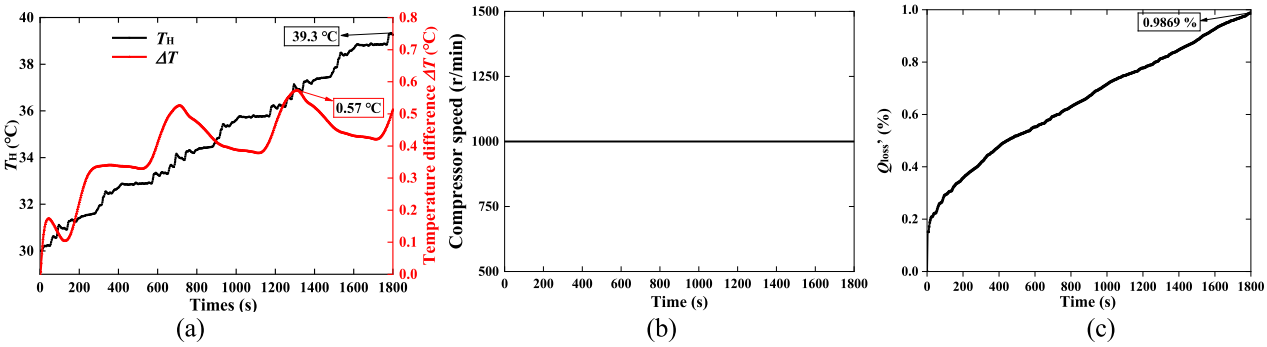

FIGURE 17. Optimization results of the minimum energy consumption control strategy: (a) The temperature (T_H) of the battery module with the highest temperature in battery pack and the temperature difference ΔT, (b) compressor speed, (c) battery aging losses Q_{loss}'.

the heat transfer rate in the chiller, so, the greater the temperature difference between the inlet and outlet of the coolant. Therefore, the temperature difference between the modules will increase.

B. COMPARISON OF THE PHASED CONTROL STRATEGY AND THE CONSTANT SPEED CONTROL STRATEGY

It can be seen from Fig. 14 that under the condition of a constant compressor speed, when the coolant flow rate is greater than 8 L/min, $(T_H)_{max}$ and $(\Delta T)_{max}$ no longer decrease obviously, which indicates that the cooling performance has reached saturation. Therefore, in the following simulation analysis, the coolant flow rate was selected to be 8 L/min.

The temperature interval in the phased control strategy of Section IV can be divided into five intervals: $T_1 \leq 30°C$, $T_2 = 30°C$, $T_3 = 32°C$, $T_4 = 34°C$, and $T_5 = 36°C$; that is, $T \leq 30°C$, $30\ °C < T \leq 32°C$, $32°C < T \leq 34°C$, $34°C < T \leq 36°C$, and $T > 36°C$. The decision variables corresponding to the five intervals are n_1, n_2, n_3, n_4, and n_5, respectively. In addition, each decision variable n_i is optimized by genetic algorithm.

The phased control strategy and the traditional constant speed control strategy are adopted to cool the battery pack. Under the same conditions, the average temperature of the T_H as the optimization parameter, and it was set to about 32.5 °C. The reason why the average temperature was chosen as the optimization parameter was because the Q_{loss}' was calculated using the average temperature. The simulation results of the two control strategies are shown in Fig. 16, which respectively shows the change of the T_H (temperature of the battery module with the highest temperature in battery pack), the change of the ΔT (temperature difference between modules in battery pack.), and the change of compressor speed. On constant speed control strategy, the compressor speed is kept at 2300 r/min, the maximum temperature is 34.9 °C, the maximum temperature difference is 1.23 °C, and the energy consumption of compressor is 0.449 KW·h. On phased control strategy, the compressor speed varies according to the battery temperature, the maximum temperature is 34.8 °C, the maximum temperature difference is 1.22 °C, and the energy consumption is 0.401 KW·h. As can be seen from Fig. 16 (b), the heat accumulation in battery pack is small at the early period, so the smaller compressor speed can meet the cooling require-

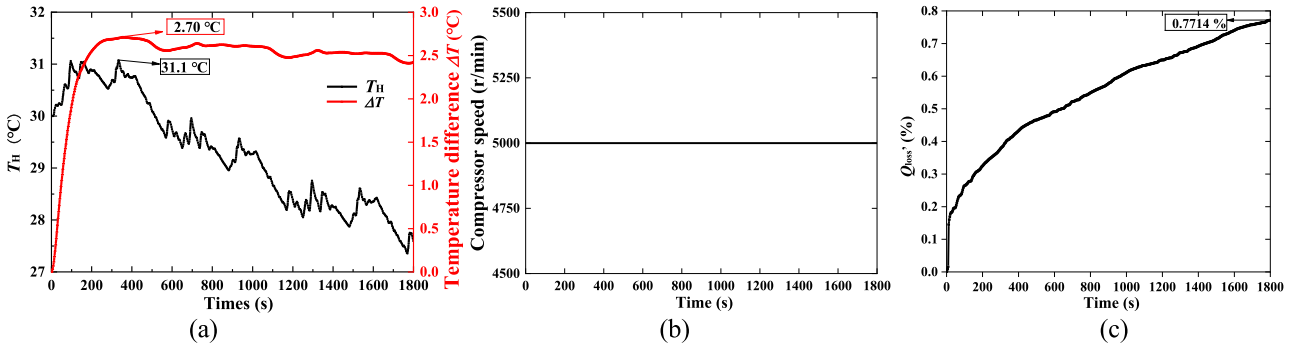

FIGURE 18. Optimization results of the minimum aging losses control strategy: (a) The temperature (T_H) of the battery module with the highest temperature in battery pack and the temperature difference ΔT, (b) compressor speed, (c) battery aging losses Q_{loss}'.

TABLE 5. The comparison of simulation results between the phased control strategy and the constant speed control strategy.

Strategies	average temperature	$(T_H)_{max}$	$(\Delta T)_{max}$	Compressor speed	energy consumption
Phased control strategy	32.5 °C	34.8 °C	1.22 °C	Fig. 16 (b)	0.401 KW·h
Constant speed control strategy	32.5 °C	34.9 °C	1.23 °C	2300 r/min	0.449 KW·h

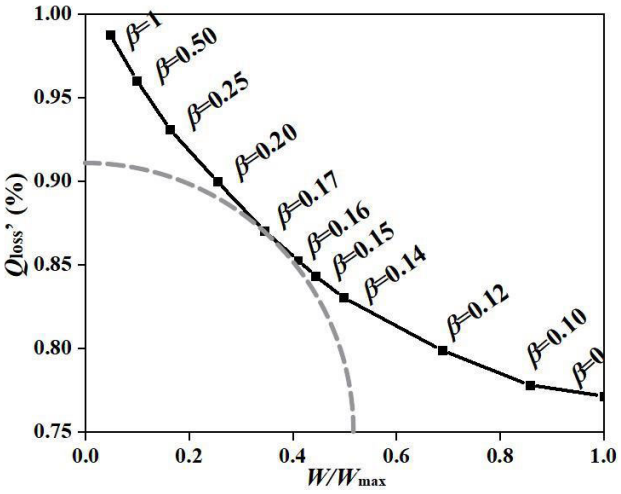

FIGURE 19. Pareto Frontier under different weight coefficients.

ments. At 1536 s, the compressor speed of the phased control strategy reaches 2332 r/min, and the temperature begins to fall below the constant speed control strategy's temperature. Under the same conditions, the energy consumption of the phased control strategy is reduced by 10.7% compared to the constant speed control strategy. Therefore, the phased control strategy proposed in this paper can effectively decrease the system's energy consumption. The comparison of the simulation results of the phased control strategy and constant speed control strategy is shown in table 5.

C. MULTI-OBJECTIVE OPTIMIZATION SIMULATION RESULTS

The energy consumption of the compressor and the aging losses of the battery are both optimization goals, which constitutes a multi-objective optimization problem. The genetic algorithm is used for the optimization. When the weight coefficient β takes different values, different control strategies can be obtained.

1) MINIMUM ENERGY CONSUMPTION CONTROL STRATEGY

β is the weight coefficient for compressor energy consumption, when $\beta = 1$, the system's energy consumption is minimum, so the optimization goal becomes: $J = \min f = \min W/W_{max}$, that is, the aging losses of the battery are not considered. The optimization results of the genetic algorithm are shown in Fig. 17. When only pursuing the lowest energy consumption, the compressor will keep running at the lowest speed, regardless of the temperature range, as shown in Fig. 17 (b), where compressor speed n is 1000 r/min. To achieve the goal of minimum energy consumption, the compressor speed does not change according to the temperature intervals, and the final energy consumption $W/W_{max} = 0.047$, and $W = 0.073$ KW·h. In this case, the temperature will always rise, the maximum temperature reaches 39.3 °C, the maximum temperature difference is 0.57 °C, and the final aging losses $Q'_{loss} = 0.9869\%$.

2) MINIMUM AGING LOSSES CONTROL STRATEGY

When $\beta = 0$, that is, the weight coefficient of the energy consumption is 0, the energy consumption is not considered. Therefore, the optimization goal becomes: $J = \min f = \min Q_{loss}$', only pursuing the lowest aging losses. The optimization results are shown in Fig. 18, where the maximum temperature of the battery is 31.1 °C, the maximum temperature difference is 2.70 °C, and the final aging losses $Q'_{loss} = 0.7714\%$. It can be seen from (12) that, under certain conditions, the aging losses and the temperature are inversely related. Therefore, in this case, where the battery aging losses

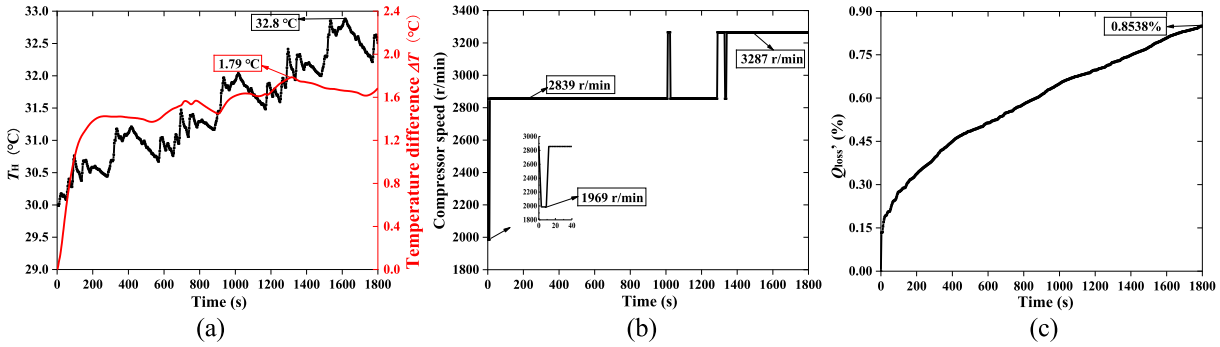

FIGURE 20. Optimization results of the balanced control strategy: (a) The temperature (T_H) of the battery module with the highest temperature in battery pack and the temperature difference ΔT, (b) compressor speed, (c) battery aging losses Q_{loss}'.

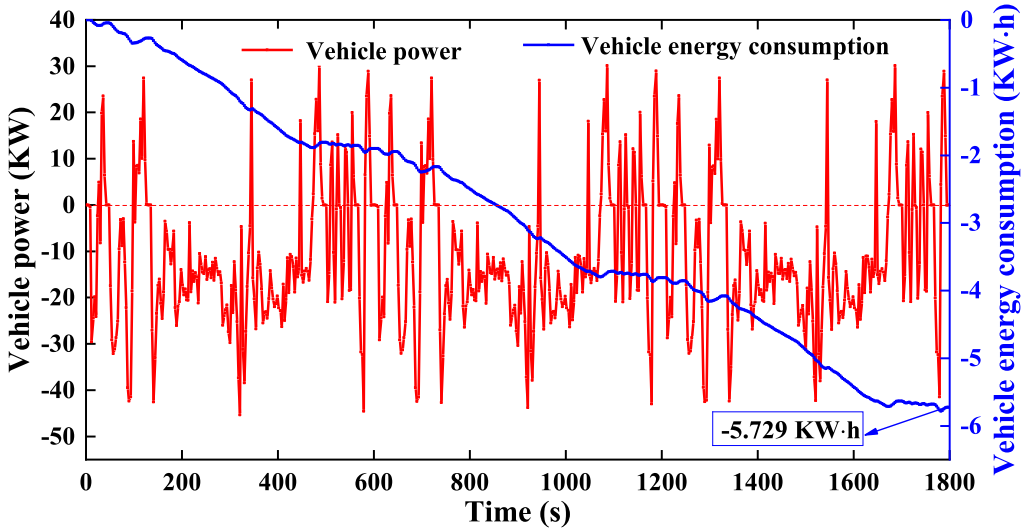

FIGURE 21. Vehicle power and energy consumption during driving.

are minimized, the system will operate at the maximum compressor speed, so that the battery temperature is as low as possible. Therefore, as seen from Fig. 18 (b), the compressor speed is not switched according to different temperature intervals but is kept at 5000 r/min. The final energy consumption of the compressor is therefore $W/W_{max} = 1$, $W = 1.553$ KW·h.

3) BALANCED CONTROL STRATEGY

Under different weight coefficients, different control strategies and different optimization results will be obtained. When taking different β values, the compressor energy consumption W/W_{max} and the aging losses Q_{loss}' under the current weight coefficient are obtained, and then, they are drawn into a curve, which is the Pareto Frontier, as shown in Fig. 19. The points on the Pareto Frontier are the best results under the current weight coefficient, and it is no longer possible to obtain a gain in an optimization goal without damaging another optimization goal. It can be seen from Fig. 19 that the two optimization goals W/W_{max} and Q_{loss}' are conflicting, so it is impossible for both to reach the optimal value. However, these two optimization goals have higher sensitivities, as long as the pursuit of the lower energy consumption gain can obtain more aging losses gain, that is, at the expense of less energy consumption, more battery cycle life can be obtained. Therefore, there is an optimal weighting coefficient, which makes both optimization goals W/W_{max} and Q_{loss}' relatively better and the overall benefits the highest.

From the Pareto Frontier, the optimal β value can be obtained. It can be seen from Fig. 19 that when $\beta = 0.17$, the overall benefits are the highest, the control strategy obtained at this case is called the balanced control strategy. The balanced control strategy's simulation results are shown in Fig. 20, where the energy consumption W/W_{max} is 0.387, $w = 0.601$ KW·h, the battery aging losses $Q'_{loss} = 0.8538\%$, the maximum temperature is 32.8 °C, the maximum temperature difference is 1.79 °C, and the compressor speed change as shown in Fig. 20 (b). Compared with the minimum energy consumption control strategy $W/W_{max} = 0.047$, the W/W_{max} of the balance control strategy is 0.387, which increases by 34.0%. But the aging loss Q_{loss}' of the latter

is reduced by 0.1331%. Therefore, the Q_{loss}' of the balance control strategy is reduced by 61.8% compared with the total reduction of aging losses, that is, the difference in Q_{loss}' between the minimum energy consumption control strategy and the minimum aging losses control strategy.

Fig. 21 shows the vehicle power and the energy consumption of the whole driving cycle under the balance control strategy. Negative power indicates energy consumption, and positive power indicates vehicle braking energy recovery. The final energy consumption is 5.729 KW·h. As mentioned earlier, the balanced control strategy increased the compressor energy consumption by 34.0%, 0.528 KW·h, compared with the minimum energy consumption control strategy. This increased compressor energy consumption is only 9.22% of the energy consumption of vehicle whole driving cycle, that is, only 9.22% of driving mileage is sacrificed, and 61.8% of battery aging losses can be reduced. It is worth mentioning that the aging loss of the battery is an irreversible and permanent attenuation of the maximum battery capacity. Reducing the aging loss of the battery is of great significance for the long-term use of electric vehicles. Therefore, the balanced control strategy can make the two optimization goals have the highest overall gain, increase the small energy consumption, and obtain a large battery life gain.

VI. CONCLUSION

A secondary loop cooling scheme is used for the battery thermal management system in this paper, and the research object is the battery pack, so the temperature control of the cabin is not mentioned. Mathematical models of key components in the thermal management system are established and experimentally verified. Based on this, a phased control strategy for adjusting the compressor speed according to the battery temperature interval is proposed. The compressor speed as the decision variable, and the compressor energy consumption and battery aging loss are used as the optimization goals. Then the genetic algorithm is adopted to solve the multi-objective optimization model.

The following key findings are observed:

1) The influence of compressor speed and coolant flow rate on battery maximum temperature and temperature difference are analyzed. Simulation results show that the compressor speed has a significant effect on maximum temperature and temperature difference. Under a certain compressor speed, the maximum temperature and temperature difference will reach a minimum value instead of decreasing all the time increases with coolant flow rate.
2) Under the same conditions, the battery average temperature was controlled at 32.5 °C, the energy consumption of the phased control strategy was reduced by 10.7% compared to the constant speed control strategy.
3) The Pareto Frontier under different weight coefficients is established. The minimum energy consumption control strategy ($\beta = 1$), the minimum aging losses control strategy ($\beta = 0$) and the balance control strategy ($\beta = 0.17$) are analyzed specially. The simulation results show that the maximum temperature in battery pack of the three control strategies is less than 40 °C, and the maximum temperature difference is less than 5 °C.
4) On the balance control strategy, the compressor energy consumption $W = 0.601$ KW·h, and the battery aging losses $Q'_{\text{loss}} = 0.8538\%$. Under the balance control strategy, only sacrificing 9.22% of the mileage of the vehicle, the battery aging losses can be reduced by 61.8%, and a substantial battery life gain can be obtained. Overall considering vehicle mileage and battery life, the balance control strategy can get higher overall benefits.

Based on the above researching achievements, the experimental verification for the phased control strategy will be carried out in next step. In addition, in order to obtain a more accurate thermoelectric aging coupling model, considering the feedback effect of the aging model on the electrical and thermal models will be done in the next step.

REFERENCES

[1] N. O. Moraga, J. P. Xamán, and R. H. Araya, "Cooling li-ion batteries of racing solar car by using multiple phase change materials," *Appl. Thermal Eng.*, vol. 108, pp. 1041–1054, Sep. 2016.

[2] A. A. Pesaran, "Battery thermal models for hybrid vehicle simulations," *J. Power Sour.*, vol. 110, pp. 377–382, Aug. 2002.

[3] P. Ramadass, B. Haran, R. White, and B. N. Popov, "Capacity fade of sony 18650 cells cycled at elevated temperatures," *J. Power Sour.*, vol. 112, no. 2, pp. 614–620, Nov. 2002.

[4] R. Mahamud and C. Park, "Reciprocating air flow for li-ion battery thermal management to improve temperature uniformity," *J. Power Sour.*, vol. 196, no. 13, pp. 5685–5696, Jul. 2011.

[5] N. Yang, X. Zhang, G. Li, and D. Hua, "Assessment of the forced air-cooling performance for cylindrical lithium-ion battery packs: A comparative analysis between aligned and staggered cell arrangements," *Appl. Thermal Eng.*, vol. 80, pp. 55–65, Apr. 2015.

[6] Y. Huo and Z. Rao, "The numerical investigation of nanofluid based cylinder battery thermal management using lattice Boltzmann method," *Int. J. Heat Mass Transf.*, vol. 91, pp. 374–384, Dec. 2015.

[7] J. Zhao, Z. Rao, and Y. Li, "Thermal performance of mini-channel liquid cooled cylinder based battery thermal management for cylindrical lithium-ion power battery," *Energy Convers. Manage.*, vol. 103, pp. 157–165, Oct. 2015.

[8] Y. Lv, X. Yang, G. Zhang, and X. Li, "Experimental research on the effective heating strategies for a phase change material based power battery module," *Int. J. Heat Mass Transf.*, vol. 128, pp. 392–400, Jan. 2019.

[9] W. Wang, X. Zhang, C. Xin, and Z. Rao, "An experimental study on thermal management of lithium ion battery packs using an improved passive method," *Appl. Thermal Eng.*, vol. 134, pp. 163–170, Apr. 2018.

[10] N. Putra, B. Ariantara, and R. A. Pamungkas, "Experimental investigation on performance of lithium-ion battery thermal management system using flat plate loop heat pipe for electric vehicle application," *Appl. Thermal Eng.*, vol. 99, pp. 784–789, Apr. 2016.

[11] Q. Wang, Z. Rao, Y. Huo, and S. Wang, "Thermal performance of phase change material/oscillating heat pipe-based battery thermal management system," *Int. J. Thermal Sci.*, vol. 102, pp. 9–16, Apr. 2016.

[12] J. Zhao, Z. Rao, Y. Huo, X. Liu, and Y. Li, "Thermal management of cylindrical power battery module for extending the life of new energy electric vehicles," *Appl. Thermal Eng.*, vol. 85, pp. 33–43, Jun. 2015.

[13] D. Chen, J. Jiang, G.-H. Kim, C. Yang, and A. Pesaran, "Comparison of different cooling methods for lithium ion battery cells," *Appl. Thermal Eng.*, vol. 94, pp. 846–854, Feb. 2016.

[14] H. Hirano, T. Tajima, T. Hasegawa, T. Sekiguchi, and M. Uchino, "Boiling liquid battery cooling for electric vehicle," in *Proc. IEEE Conf. Expo Transp. Electrific. Asia–Pacific (ITEC Asia–Pacific)*, Aug. 2014, pp. 1–4.
[15] G. Xia, L. Cao, and G. Bi, "A review on battery thermal management in electric vehicle application," *J. Power Sour.*, vol. 367, pp. 90–105, Nov. 2017.
[16] T. Zhang, Q. Gao, G. Wang, Y. Gu, Y. Wang, W. Bao, and D. Zhang, "Investigation on the promotion of temperature uniformity for the designed battery pack with liquid flow in cooling process," *Appl. Thermal Eng.*, vol. 116, pp. 655–662, Apr. 2017.
[17] P. Goli, S. Legedza, A. Dhar, R. Salgado, J. Renteria, and A. A. Balandin, "Graphene-enhanced hybrid phase change materials for thermal management of li-ion batteries," *J. Power Sour.*, vol. 248, pp. 37–43, Feb. 2014.
[18] T.-H. Tran, S. Harmand, B. Desmet, and S. Filangi, "Experimental investigation on the feasibility of heat pipe cooling for HEV/EV lithium-ion battery," *Appl. Thermal Eng.*, vol. 63, no. 2, pp. 551–558, Feb. 2014.
[19] H. S. Hamut, I. Dincer, and G. F. Naterer, "Exergy analysis of a TMS (thermal management system) for range-extended EVs (electric vehicles)," *Energy*, vol. 46, no. 1, pp. 117–125, Oct. 2012.
[20] M. Shen and Q. Gao, "System simulation on refrigerant-based battery thermal management technology for electric vehicles," *Energy Convers. Manage.*, vol. 203, Jan. 2020, Art. no. 112176.
[21] J. Min, Z. Zhiguo, and C. Xiang, "Design and research on battery thermal management system for hybrid electric vehicles," *Appl. Energy Technol.*, vol. 250, no. 10, pp. 1–4, 2018.
[22] W. Qiuxia, "Research on the thermal management strategy of lithium power battery management system," *Mech. Electr. Eng. Technol.*, vol. 45, no. 9, pp. 65–68, 2016.
[23] F. He and L. Ma, "Thermal management of batteries employing active temperature control and reciprocating cooling flow," *Int. J. Heat Mass Transf.*, vol. 83, pp. 164–172, Apr. 2015.
[24] L. Wei, "Heat transfer analysis and control method research on liquid cooling system for power battery pack," M.S. thesis, Dept. Jilin Univ., Jilin, China, 2016.
[25] R. Wang and S. M. Lukic, "Dynamic programming technique in hybrid electric vehicle optimization," in *Proc. IEEE Int. Electr. Vehicle Conf.*, Mar. 2012, pp. 1–8.
[26] J.-Q. Li, X. Jin, and R. Xiong, "Multi-objective optimal energy management strategy and economic analysis for an range-extended electric bus," *Energy Procedia*, vol. 88, pp. 814–820, Jun. 2016.
[27] C. Zhu, F. Lu, H. Zhang, J. Sun, and C. C. Mi, "A real-time battery thermal management strategy for connected and automated hybrid electric vehicles (CAHEVs) based on iterative dynamic programming," *IEEE Trans. Veh. Technol.*, vol. 67, no. 9, pp. 8077–8084, Sep. 2018.
[28] J. Jaguemont, L. Boulon, Y. Dube, and F. Martel, "Thermal management of a hybrid electric vehicle in cold weather," *IEEE Trans. Energy Convers.*, vol. 31, no. 3, pp. 1110–1120, Sep. 2016.
[29] S. Bauer, A. Suchaneck, and F. Puente León, "Thermal and energy battery management optimization in electric vehicles using Pontryagin's maximum principle," *J. Power Sour.*, vol. 246, pp. 808–818, Jan. 2014.
[30] T. Yuksel, S. Litster, V. Viswanathan, and J. J. Michalek, "Plug-in hybrid electric vehicle LiFePO4 battery life implications of thermal management, driving conditions, and regional climate," *J. Power Sour.*, vol. 338, pp. 49–64, Jan. 2017.
[31] C. Zhu, F. Lu, H. Zhang, K. Zhu, and C. Mi, "A finite-set model-based predictive battery thermal management in connected and automated hybrid electric vehicles," in *Proc. IEEE Appl. Power Electron. Conf. Exposit. (APEC)*, Mar. 2018, pp. 3428–3433.
[32] W. Kairong, *Optimization Method*. Beijing, China: Science Press, 2012.
[33] Q.-K. Wang, Y.-J. He, J.-N. Shen, Z.-F. Ma, and G.-B. Zhong, "A unified modeling framework for lithium-ion batteries: An artificial neural network based thermal coupled equivalent circuit model approach," *Energy*, vol. 138, pp. 118–132, Nov. 2017.
[34] Y. Xie, W. Li, Y. Yang, and F. Feng, "A novel resistance-based thermal model for lithium-ion batteries," *Int. J. Energy Res.*, vol. 42, no. 14, pp. 4481–4498, Nov. 2018.
[35] Y. Shiming and T. Wenquan, *Heat Transfer*, 2nd ed. Beijing, China: Higher Education Press, 2006.
[36] J. Wang, P. Liu, J. Hicks-Garner, E. Sherman, S. Soukiazian, M. Verbrugge, H. Tataria, J. Musser, and P. Finamore, "Cycle-life model for graphite-LiFePO$_4$ cells," *J. Power Sour.*, vol. 196, no. 8, pp. 3942–3948, Apr. 2011.
[37] M. Petit, E. Prada, and V. Sauvant-Moynot, "Development of an empirical aging model for li-ion batteries and application to assess the impact of Vehicle-to-Grid strategies on battery lifetime," *Appl. Energy*, vol. 172, pp. 398–407, Jun. 2016.
[38] M. M. Shah, "A general correlation for heat transfer during film condensation inside pipes," *Int. J. Heat Mass Transf.*, vol. 22, no. 4, pp. 547–556, Apr. 1979.
[39] F. Schmidt, *VDI Atlas—Part L2.4 Calculating Critical Mass Flux*, 2nd ed. Berlin, Germany: Springer-Verlag, 2010.
[40] W. Guohua, "Research on thermal management system cooling modeling and battery thermal control strategy," Ph.D. dissertation, Dept. Jilin Univ., Jilin, China, 2017.

XIJIN KUANG received the B.E. degree in energy and power engineering from Jiangsu University, Jiangsu, China, in 2017. He is currently pursuing the M.S. degree in energy and power engineering with Chongqing University.

KUINING LI received the M.S. degree in thermal engineering and the Ph.D. degree in engineering thermophysics from Chongqing University, Chongqing, China, in 1997 and 2003, respectively. He is currently a Professor with the School of Energy and Power Engineering, Chongqing University. He has led and has been involved in more than 13 research projects, such as the National Key Research and Development Program, the Natural Science Foundation of China, and so on. He has published more than 40 articles. His research interests include thermal management of lithium-ion batteries, thermal management of EVs, and intelligent air conditioning system for vehicles.

YI XIE received the B.E. degree in power engineering from North China Electrical Power University, Beijing, China, in 2006, and the Ph.D. degree in thermal power engineering from the School of Energy and Power Engineering, Beihang University, in 2012. He is currently an Associate Professor with the School of Automotive Engineering, Chongqing University, Chongqing, China. He has led and has been involved in more than 15 research projects, such as the National Key Research and Deveopment Program, the National Natural Science Foundation of China, and so on. He has published more than 30 articles. His research interests include thermal management of lithium-ion batteries, thermal management of EVs, and intelligent air conditioning system for vehicles.

CUNXUE WU received the M.S. degree in mechanical engineering from Chongqing University, Chongqing, China, in 2005, where he is currently pursuing the Ph.D. degree in automotive engineering. He is currently a Manager with the Chongqing Chang'an New Energy Automotive Technology Company Ltd. He had led several projects involving electromagnetic compatibility, durability test of electronic module, HIL test of the vehicle, body control, and engine control.

PINGZHONG WANG received the B.E. degree in polymer materials engineering from Northeast Forestry University, Harbin, China, in 2008. He is currently the Head of the Intelligent Business Unit and Thermal Management System Room, Chongqing Chang'an New Energy Automotive Technology Company Ltd. He has participated in more than three national and municipal scientific research projects. His research interests include thermal management of EVs and intelligent air conditioning system for vehicles.

XIAOBO WANG received the M.S. degree in thermal energy and power engineering from the Beijing Institute of Technology, Beijing, China, in 2013. He is currently a Senior Engineer with Chang'an New Energy Automotive Technology Company Ltd., where he is responsible of the vehicle thermal management. He has participated in more than three national and municipal scientific research projects.

CHUNYUN FU received the B.E. degree from Chongqing University, China, in 2010, and the Ph.D. degree from RMIT University, Australia, in 2015. He is currently a Lecturer with the School of Automotive Engineering, Chongqing University. His research interests include electric vehicles and autonomous vehicles.